International Journal of Solids and Structures 300 (2024) 112930

Contents lists available at ScienceDirect

International Journal of Solids and Structures

journal homepage: www.elsevier.com/locate/ijsolstr

A novel in-situ micro-mechanical testing of paper fracture and its stochastic network model

Mohadeseh Fallah *, Hamed Zarei, Marco Paggi

IMT School for Advanced Studies Lucca, Piazza San Francesco 19, Lucca, 55100, Italy

ARTICLE INFO

Keywords:
Fiber network material
In-situ tensile test
Confocal microscopy
Statistical model
Micromechanics

ABSTRACT

Understanding and simulating the evolution of fracture in cellulose-based paper materials is vital for many eco-sustainable applications of packaging solutions. In this work, we conduct an integrated experimental-statistical mechanics analysis to elucidate how the microstructural mechanisms govern the fracture behavior of paper. We employ in-situ tensile tests combined with confocal microscopy to observe and analyze key microstructural phenomena, such as fibers' activation and recruitment, and progressive tensile failure of unnotched paper samples under uniaxal loading. The developed stochastic mechanics critical cross-section model to treat the cellulose fiber network is able to decouple the stochastic morphological parameters from the constitutive model of the fibers. Notably, it robustly predicts the anisotropic properties of paper materials in the machine direction (MD) and cross-machine direction (CD) as a direct consequence of the different statistical distribution of fibers' orientation, for the same fiber constitutive model. The proposed approach is finally employed to get an insight into the role of the main morphological parameters, local/non-local fibers' strain redistribution, and finite elasticity of fibers on the whole mechanical behavior of paper.

1. Introduction

Paper materials exhibit a complex material micro-structure, consisting of fibers pressed together and interacting within a network. These cellulose-based materials during their deformation involve phenomena occurring across multiple length scales, from the nanometer-scale interactions between cellulose fibers to the macro-scale behavior of the entire sheet. Therefore, in order to capture the complex interactions at different scales (the fiber scale, the network scale, and the sheet scale) for the paper materials, multiscale modeling is an emerging research field (Simon, 2021). Over the years, researchers have performed significant research on computational modeling of paper materials. One notable approach involves finite element modeling, used to simulate how paper behaves under different conditions (Brandberg et al., 2022; Kloppenburg et al., 2023b; Kulachenko and Uesaka, 2012; Shahsavari and Picu, 2013; Tojaga et al., 2021; Torgnysdotter et al., 2007a,b). These computational models allowed researchers to explore the mechanical properties of paper materials, but simulating and analyzing a fiber network at the macroscale becomes computationally expensive due to the inherent complexity of these random networks composed of thousands of fibers. Consequently, researchers commonly employ a Representative Volume Element (RVE) to capture the material's macrostructural behavior and reduce the computational cost. However, the size of the RVE has emerged as a critical factor in accurately representing the material behavior of the macrostructure, a subject that has been investigated in depth and discussed by Kloppenburg et al. (2023b), Li et al. (2018), Shahsavari and Picu (2013). Moreover, homogenization approaches cannot be invoked when strain localization takes place, as occurs at the peak load and in the post-peak branch of the force–displacement curve due to crack growth.

The mechanical characteristics of paper materials as fiber networks are known to be influenced significantly by interactions between fibers and the properties of individual fibers. These attributes, including densities and distribution of fibers segment lengths and their geometrical properties, have been shown to undergo statistical changes within a fiber network (Alava and Niskanen, 2006; Dodson and Sampson, 1999; Yi et al., 2004). Consequently, in this work, we are going to introduce a statistical mechanics theoretical model and its numerical implementation designed not only for efficient computational modeling of fiber networks at the macroscale, but also for accurate prediction of their fracture along a critical cross-section by including all the microscale features, without limitations on the number of fibers to be simulated. In parallel, in-situ experimental testing is proposed by conducting tensile test and observing the material evolution under loading, examining the microscopical phenomena involved during deformation up to fracture. Researchers have done some micromechanical tests for

* Corresponding author.
E-mail address: mohadeseh.fallah@imtlucca.it (M. Fallah).

https://doi.org/10.1016/j.ijsolstr.2024.112930
Received 5 April 2024; Received in revised form 21 May 2024; Accepted 11 June 2024
Available online 20 June 2024

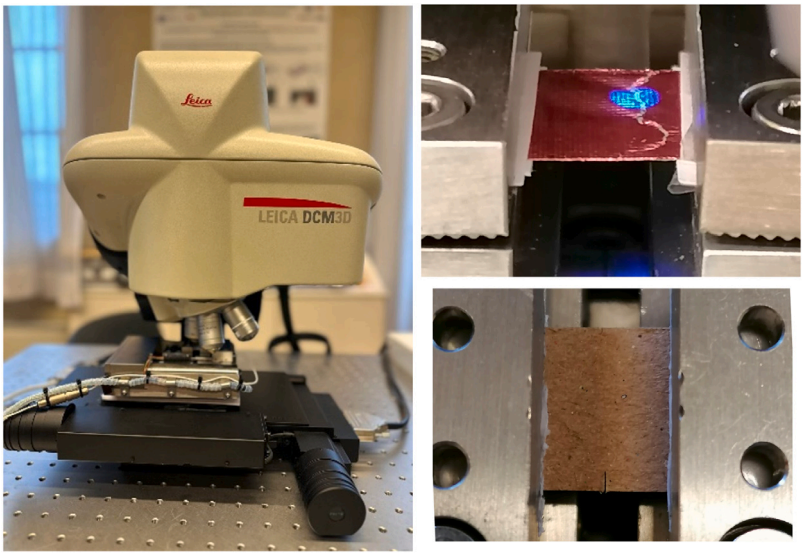

Fig. 1. In-situ micro-mechanical tensile testing setup: DEBEN micro-mechanical tensile stage and the Leica DCM3D confocal microscope (left panel); photos of unnotched Al-paper laminate (right panel, top) and notched paper (right panel, bottom) specimens that can be tested in uniaxial tension with this equipment.

the characterization of fiber properties (El-Hosseiny and Page, 1975; Groom et al., 2002; Maraghechi et al., 2023). However, in the context of paper materials, results regarding in-situ testing are quite scarce. Therefore, we propose an experimental campaign by combining the micromechanical tensile stage (DEBEN) and the confocal microscope (Leica DCM3D) with a setup which offers a versatile way to explore the microstructural mechanisms responsible for fracture.

This article is organized as follows. In the Methodology section, we begin by detailing the experimental setup and highlighting key observations made during experiments. Subsequently, we introduce a statistical mechanics model of a critical cross-section for predicting the fracture behavior of paper materials, encompassing both the theoretical formulation and the algorithmic aspects. The model parameters section provides an extensive discussion on how to determine and validate the parameters entering the proposed model. In the sensitivity analysis section, we employ the developed model to explore the influence of various parameters on the mechanical response of paper materials, to gain further insight into the micromechanical mechanisms governing paper fracture. Lastly, main conclusions and future developments are summarized in the Conclusion section.

2. Experimental methods: in-situ material testing setup

The equipment includes the micro-mechanical tensile stage DEBEN placed under the confocal microscope Leica DCM3D, see Fig. 1, both available in the MUSAM-Lab of the IMT School for Advanced Studies Lucca. This setup allows the in-situ visualization of the cellulose fibers and also the out-of-plane deformation of the specimen surface during the whole loading history (Johansson et al., 2022), while the force–displacement curve is progressively recorded by the tensile stage.

A series of uniaxial tensile tests on unnotched rectangular paper specimens with dimensions $B \times L \times t$ (width, span and thickness) has been carried out. The specimens have been clamped at the extremes. The displacement loading rate has been set equal to 0.1 mm/min, which is sufficiently low to monitor all the micromechanical damage phenomena with the confocal microscope and perform a single test in a reasonable amount of time. As exemplified in Fig. 2, single cellulose fibers that bridge a propagating crack can be clearly observed, as well as those debonded and broken.

Furthermore, the employed tensile stage allows us to determine the overall mechanical behavior of paper -which is an emergent mechanical response- by measuring the force–displacement curve under displacement control which is of the type depicted in Fig. 4 (paper tested in the cross-machine CD direction). The response is initially linear and then it departs from linearity up to reaching a maximum load carrying capacity. After the peak load, a sharp softening branch takes place. This mechanical response, which can be converted into a conventional stress–strain diagram by dividing the force by the cross-section area and the displacement by the initial free span, has been recently interpreted through a phase field model for fracture driven by elastoplasticity with hardening (Marengo, 2023). However, the present authors consider this modeling assumption quite controversial, since the observed microscopical mechanisms do not always support a continuum model ruled by elastoplastic hardening. The mechanical system is in fact composed by a discrete set of cellulose fibers with strong adhesion between them caused by the pressure acted during production. When subject to tensile loading, fibers can partially move and align along the loading direction depending on the free length of each fiber intercurring between two subsequent fiber bonds. This leads to a phenomenon which is similar to *fiber recruitment* in biological tissues (Gizzi et al., 2014; He and Lu, 2022; Li and Holzapfel, 2019).

It should be noted that fiber recruitment can occur at different loading levels depending on the fibers network and its density. In denser fiber networks, such as paper, we anticipate that fiber recruitment happens at very low strains due to the restricted deformability of individual fibers. Conversely, in rarefied networks, like those obtained by electrospinning, fiber recruitment takes place at very large strains, see Fig. 3 where a representative fiber is colored in yellow to visualize its recruitment and realignment (tensile tests on PLLA electrospun layers using the DEBEN microtensile stage placed within the SEM Zeiss EVO MA15 at the MUSAM-Lab to achieve the required resolution).

The fiber inclination is therefore relevant, since the fibers initially aligned along the loading direction mostly contribute to the load-carrying capacity. The fiber recruitment process continues until fiber slippage and bond failure is triggered. In some circumstances, fibers do not only slip with respect to each other, but also individually break, which is a catastrophic phenomenon leading to load redistribution to the remaining active fibers. These phenomena observed in our tests on paper are consistent with the microscopical mechanisms reported in the literature (Borodulina et al., 2012; Kouko et al., 2020). Recent investigations (Maraghechi et al., 2023) on single cellulose fibers tested under uniaxial test using an equipment similar to our setup showed that the slope of the stress–strain curves gradually decreases with increasing strain as a result of the development of inelastic deformations caused by micro-damage, up to the stage at which the fiber breaks.

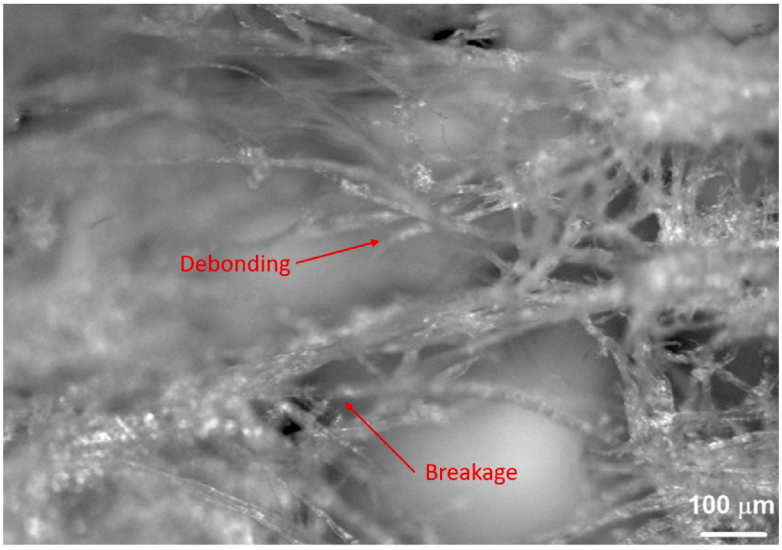

Fig. 2. Microstructural alterations within a localized specimen region after reaching a defined load threshold during tensile testing, including fiber debonding and breakage, taken by confocal microscopy (20x magnification).

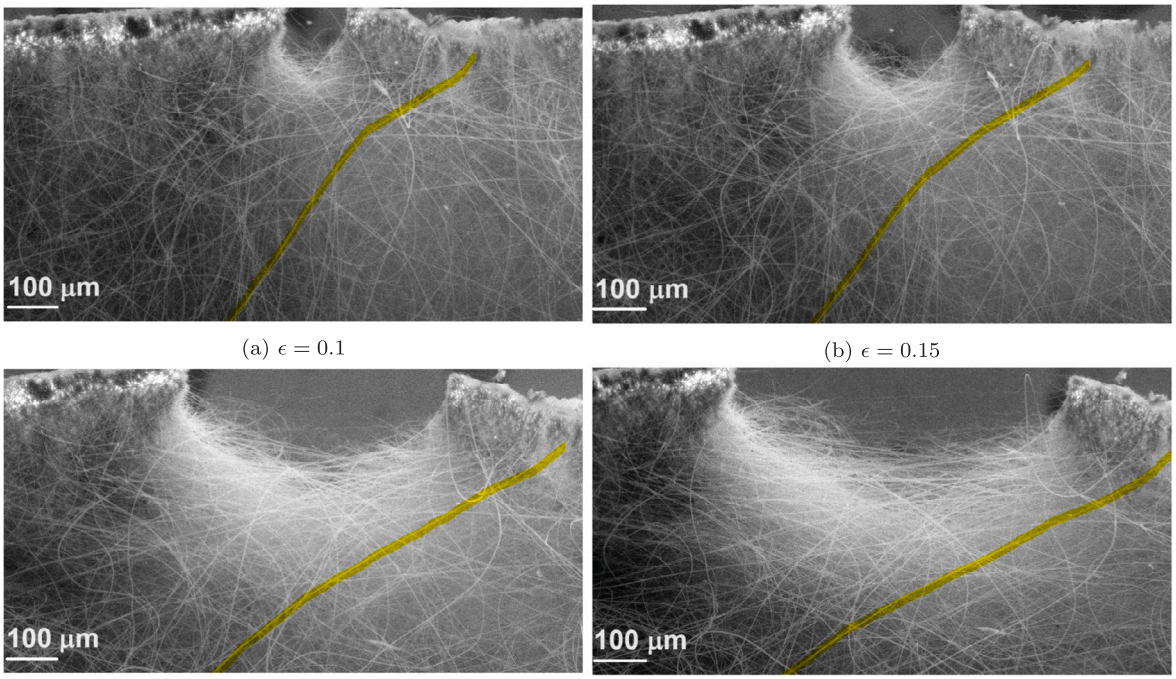

(a) $\epsilon = 0.1$ (b) $\epsilon = 0.15$

(c) $\epsilon = 0.2$ (d) $\epsilon = 0.25$

Fig. 3. SEM images of PLLA electrospun layers at different strain levels, showing fiber recruitment and realignment along the axial (horizontal) direction of loading.

Furthermore, micro-plasticity was observed in Maraghechi et al. (2023) as a mechanism typical of polymer fibers, which inherently possess a distinct composition as compared to cellulose fibers that mostly behave linear elastically.

Hence, to elucidate on these fundamental modeling assumptions and derive a model that could predict the response as a direct consequence of quantifiable and observable microscopical mechanisms involving the network of fibers, a statistical mechanics model is put forward in the next section. As shown by Borri et al. (2016), Paggi and Reinoso (2015) for the problem of adhesion between paper tissues, the stochastic features of the fiber population play an essential role for a predictive model. Here, all the model parameters related to the random network topography will be estimated from data measurable from confocal images, leaving to be identified only few parameters describing the single fiber mechanical response, which is the key controversial aspect to be assessed.

3. Statistical mechanics model

In this section, we propose a model based on the network of cellulose fibers to simulate deformation and fracture of paper subject to uniaxial loading.

The starting point is a rectangular specimen of paper of $B \times L \times t$ dimensions, where B is its width, L its span, and t is its thickness. An orthogonal $x - y - z$ reference system is also introduced and an axial displacement w is applied along the $z-$direction (see the sketch in Fig. 5).

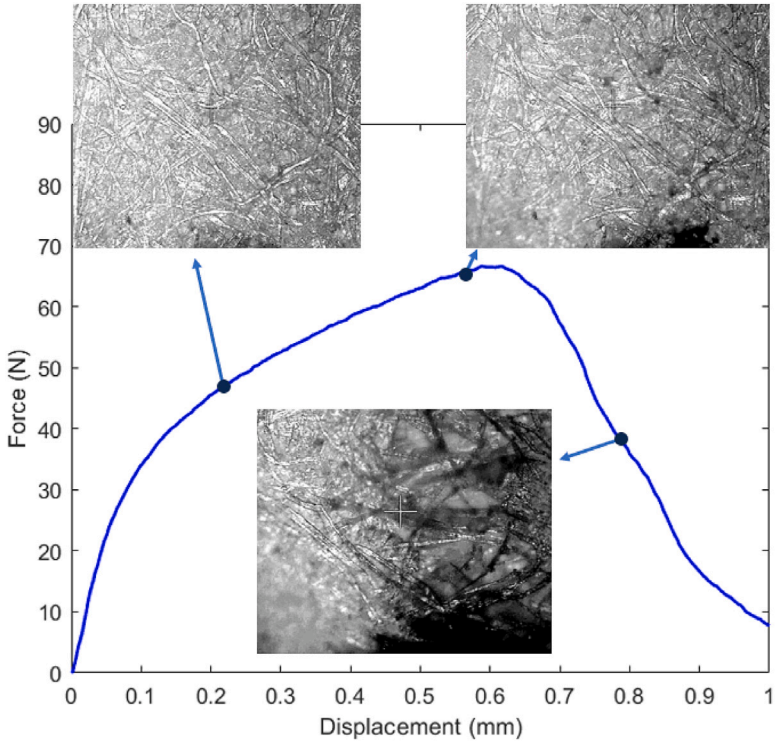

Fig. 4. A typical mechanical response of a paper sample under tensile loading in the cross-machine direction (CD), with fiber recruitment followed by fiber debonding and slippage during crack growth. A video of the test is available as an electronic supplementary material.

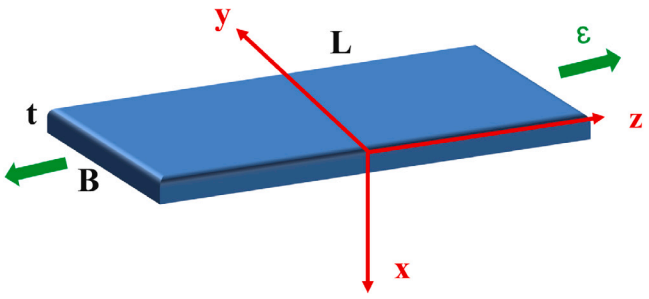

Fig. 5. Schematic of the specimen and load orientation with respect to a global reference system.

Under a macroscopically applied strain, $\epsilon = w/L$, resulting from the imposed displacement w, fracture may occur at a randomly located single critical cross-section. Notably, the experimental tensile tests performed on both short-span and long-span specimens (referenced in Marengo (2023)) demonstrate a variation in the force–displacement curves. These variations regard a simple linear scaling of the displacement with L, while forces do not change. This supports our model assumption that a cross-sectional model is adequate to describe the response of paper under uniaxial tension, where fracture occurs primarily at a single cross-section. Hence, under these assumptions, it is possible to focus the attention on the behavior of fibers crossing that representative cross-section. First, the average total number of fibers along such a cross-section can be quantified as:

$$N = N_l N_f \tag{1}$$

where N_l denotes the number of paper layers ($j = 1, \dots N_l$), each one with a thickness of a fiber, and N_f is the average number of fibers along the $y-$direction for each layer ($i = 1, \dots N_f$). Therefore, a fiber is univocally identified by the indices i and j.

At the microscale, fibers are assumed to have an average cross-section A, a random length $l_{i,j}$, and a random orientation angle $\alpha_{i,j}$ measured from the axial direction (z-axis). The centre of those fibers is placed at $x_{i,j} = jt/N_l$, $y_{i,j} = iB/N_f$, $z_{i,j} = 0$. The coordinates of the external nodes defining the beginning and the end of each fiber, see Fig. 6, are:

$$z^{(1)}_{i,j} = -l_{i,j}/2\cos(\alpha_{i,j}) \tag{2a}$$

$$y^{(1)}_{i,j} = y_{i,j} - l_{i,j}/2\sin(\alpha_{i,j}) \tag{2b}$$

$$x^{(1)}_{i,j} = x_{i,j} \tag{2c}$$

$$z^{(2)}_{i,j} = l_{i,j}/2\cos(\alpha_{i,j}) \tag{2d}$$

$$y^{(2)}_{i,j} = y_{i,j} + l_{i,j}/2\sin(\alpha_{i,j}) \tag{2e}$$

$$x^{(2)}_{i,j} = x_{i,j} \tag{2f}$$

Fibre lengths are usually not constant, and therefore a Gaussian distribution is herein introduced to assign a random length $l_{i,j}$ to each fiber, specifying in input the mean (μ_l) and the root mean square (σ_l) values of the distribution. Moreover, cut-off lengths (l_0 and $l_{\max}$) for the shortest and the longest fibres are also considered.

Fiber orientation is also a crucial parameter, since it is well-known that the macroscopic mechanical response of paper is anisotropic and it is particularly different in the machine direction (MD) and in the cross-machine direction (CD). Since this is primarily due to the different alignment of fibers caused by the machining process, we expect that the fiber orientation might strongly influence the overall mechanical response. In the present model, we explore three possible different distributions of fiber orientations along the cross-section: (*i*) uniform distribution, (*ii*) non-uniform distribution with maximum probability in the machine direction, (*iii*) non-uniform distribution with maximum probability in the cross-machine direction. In the case of uniform distribution, the orientation angle $\alpha_{i,j}$ is assigned randomly with values ranging from 0 to $\pi/2$. For cases (*ii*) and (*iii*), on the other hand, Gaussian distributions with a mean value μ_α, a root mean square σ_α,

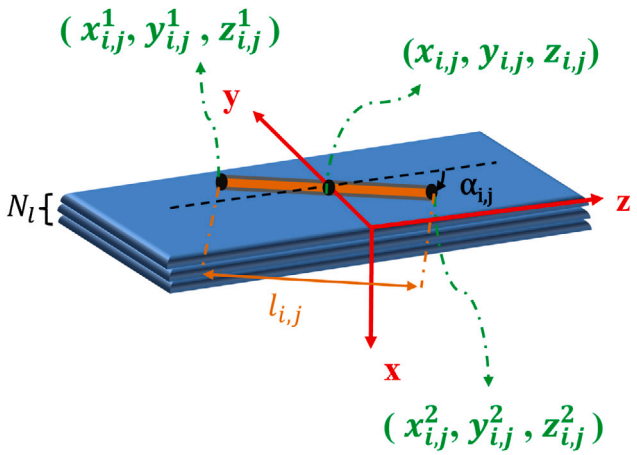

Fig. 6. Orientation and coordinated of the extremes of the fibers along the critical cross-section at the microscale.

and cut-off values $-\pi/2$ and $+\pi/2$ are considered. The mean value μ_α is set as:

$$\mu_\alpha = \begin{cases} 0, & \text{for the machine direction (MD)} \\ \pi/2, & \text{for the cross-machine direction (CD)} \end{cases} \tag{3}$$

It is worth mentioning that, considering the experimental findings by Kloppenburg et al. (2023a), which indicated fiber orientation distribution in the paper plane could resemble a normal distribution but with heavier tails, we adopt a Gaussian distribution with appropriate standard deviation and cut-off values, ensuring that the distribution does not approach zero probability for the tails. As a result, this model is capable of generating a population of fibers with different morphological characteristics, namely their lengths and orientations, representing the statistical features of paper materials.

Fibers often retain slack or curvature due to manufacturing and drying processes (Niskanen, 2011). Mechanically, a loaded fiber begins to carry the load, when it overcomes this slackness and it gets straight, which leads to a phenomenon referred to as fiber recruitment in a fibrous network. To incorporate this phenomenon into our model, we assume that a cellulose fiber within a loaded paper material is recruited when the applied strain exceeds a specified activation strain. This activation strain serves as a threshold, indicating the point at which the external strain adequately overcomes the inherent curvature or slackness in the fibers, facilitating their effective involvement in the network's load-carrying mechanism. This activation strain can be reasonably related to the distance between two bonds along a given fiber, i.e., the distance between two subsequent points where a fiber is crossed by other fibers. We believe in fact that the average distance between subsequent bonds -which is a kind of *free segment length* (Niskanen, 2011), or a *mean free path* between two bonds, λ– is responsible for the stiffness of the fiber.

Niskanen (2011) discussed the probability distribution of free segment lengths and remarked it can be assumed to be exponential with its average value λ_{avg}. Experimentally, the average mean free path can be estimated from confocal miscroscopy images by dividing a fiber length by the number of bonds observed along its length, and averaging over a statistically representative number of fibers. Hence, we can associate to each individual fiber a randomly assigned mean free path, $\lambda_{i,j}$, extracted from an exponential distribution in the range from $\lambda_{\min}$ to $\lambda_{\max}$, where $\lambda_{\max}$ and $\lambda_{\min}$ signify the maximum an minimum distance between two adjacent bonds within the network respectively, the attributes that can be effectively observed from microscopy images.

In the strain-controlled constitutive fiber model, the activation of fibers is determined based on their respective mean free paths. It is anticipated that fibers with shorter mean free paths will be activated earlier due to their relatively higher stiffness (less slackness). On the other hand, longer fibers, which may not be fully straight, do require more deformation to be engaged in the overall deformation process. Additionally, the model takes into account the connectivity of fibers, where multi-connected fibers are expected to be activated earlier than isolated ones.

To quantify the activation strain for each fiber, the following formulation is introduced:

$$\epsilon^a_{i,j} = \epsilon^{\text{act}} \left(\frac{\lambda_{i,j} - \lambda_{\min}}{\lambda_{\max} - \lambda_{\min}} \right) \tag{4}$$

where ϵ^{act} represents the maximum strain required for a fiber activation, equivalent to the strain necessary to activate a fiber possessing the maximum free path, $\lambda_{\max}$.

As cited in the literature (Li et al., 2016), since the measured force required to break the inter-fiber bond is considerably lower than the force needed for the fiber to undergo nonlinear deformation, the fiber is assumed to respond elastically after recruitment. In the uni-axial tensile test on plain specimens, with all the fibers not slipping (either not yet recruited, or recruited), the strain level ϵ is assumed to be dictated by the imposed far field displacement at the boundary, i.e., $\epsilon = w/L$. This uniform condition is then perturbed when fiber slippage takes place, and the amount of strain redistribution will be discussed later. Hence, in the linear regime, the strain applied to each fiber along its axial direction is computed from the applied strain ϵ acting on the $z-$direction:

$$\epsilon_{i,j} = \epsilon \cos(\alpha_{i,j}) \tag{5}$$

Correspondingly, the elastic force supported by the fiber is:

$$f_{i,j} = K\epsilon_{i,j} \tag{6}$$

where K is the fiber stiffness. The fiber contribution to the uni-axial load is retrieved by projecting $f_{i,j}$ back to the $z-$direction:

$$F_{i,j} = K\epsilon \cos^2(\alpha_{i,j}) \tag{7}$$

We remark here that the model can be enhanced by an elasto-plastic constitutive relation instead of a linear elastic one, simply by modifying the constitutive relation in Eq. (6). In addition, the cross-section of the fibers (A) along with Young's modulus of a single cellulose fiber, E, contribute to the calculation of the fibers' stiffness $K = EA$.

In this study, similar to the Cox model (Cox, 1952), we incorporated the orientation of fibers to facilitate load transfer among them. While the Cox model is traditionally applied to analyze fibrous materials within a resin matrix, our adaptation extends its principles to fibrous materials without a matrix. However, for such materials, the influence of bond density becomes crucial. Hence, we accounted for this factor in our model by considering the mean free length of fibres, recognizing its significance in determining the strength of these materials.

The fiber linear response is limited in the model by the strain level, when a maximum strain $\epsilon^{\max}_{i,j}$ is reached. After that level, the fiber debonds and its contribution to the overall load is assumed to be negligible. Notably, if the maximum debonding strain for each fiber, $\epsilon^{\max}_{i,j}$, exceeds the fiber's breakage strain, ϵ^{f}, then the fiber breaks before experiencing debonding. In the model, the debonding strain for each fiber is assumed to be a random field dependent upon the mean free path of the fiber, i.e.:

$$\epsilon^{\max}_{i,j} = \epsilon^{\max} \left(\frac{\lambda_{\text{avg}}}{\lambda_{i,j}} \right) \tag{8}$$

which implies that $\epsilon^{\max}$ can be estimated from the micromechanical test of bond failure with just two fibers bonded together, as for instance in Magnusson et al. (2013).

In our simulation, when a fiber undergoes failure, we adopt a strain redistribution to neighboring fibers -a strategy consistent with the principles of fiber bundle models outlined in the literature, see e.g. Pradhan et al. (2010), Pugno et al. (2012). These models, acknowledged for their

simplicity and effectiveness in understanding failure phenomena, detail the successive failure of fibers and subsequent adjustments in load redistribution among the surviving fibers. In our model, resembling these fiber bundle models, redistributing strain is functionally equivalent to redistributing load, as all fibers are assumed to have the same elastic properties. The amount of redistribution is governed in the model by a parameter r ranging from 0 to 1. If the ith fiber fails, its strain at failure will be equally redistributed to the $(i-1)$th and $(i+1)$th fibers as follows:

$$\epsilon_{i-1,j} \leftarrow \epsilon_{i-1,j} + r/2\epsilon_{i,j} \tag{9a}$$

$$\epsilon_{i+1,j} \leftarrow \epsilon_{i+1,j} + r/2\epsilon_{i,j} \tag{9b}$$

The mechanisms of fiber realignment has been found particularly relevant for the Poisson effect for the papers examined, in the range of densities. As a general trend, the lower the density, the more accurate is this assumption. As a limit case, fibrous materials obtained by electrospinning are for instance the fibrous materials where the progressive relative displacement and realignment of the fibers along the loading direction is giving the maximum contribution to the Poisson effect. By increasing the paper density, other forms of deformation of the fibers' joints may increase their role. In this study, to account also for the progressive alignment of the fibers along the direction of loading, which can lead to the macroscopic Poisson restriction effect, the z coordinates of the fiber nodes, the fiber angle and its stretched length are updated based on the deformation level (deformed configuration):

$$z_{i,j}^{(1)} \leftarrow z_{i,j} - l_{i,j}\cos(\alpha_{i,j})\epsilon_{i,j}/2 \tag{10a}$$

$$z_{i,j}^{(2)} \leftarrow z_{i,j} + l_{i,j}\cos(\alpha_{i,j})\epsilon_{i,j}/2 \tag{10b}$$

$$\alpha_{i,j} \leftarrow \arctan\left(\frac{y_{i,j}^{(2)} - y_{i,j}^{(1)}}{z_{i,j}^{(2)} - z_{i,j}^{(1)}}\right) \tag{10c}$$

$$l(i,j) \leftarrow \sqrt{\left(z_{i,j}^{(2)} - z_{i,j}^{(1)}\right)^2 + \left(y_{i,j}^{(2)} - y_{i,j}^{(1)}\right)^2} \tag{10d}$$

Consequently, we can assess the amount of realignment of fibers by calculating the norm of the difference between the fibers' orientation during the simulation with respect to the original (undeformed) one, i.e., α_0 before loading and α after loading as computed by Eq. (10), normalizing it by the total number of fibers. To quantify this effect and comparing it with the density of the networks, we anticipate that this measure of realignment in the MD direction for the materials with lower and higher densities, is equal to 1.01×10^{-4} (radians) for material 1 (the less dense paper), and 9.9×10^{-5} (radians) for material 3 (the more dense paper). These results confirm that realignment is a small quantity for paper materials, and is a decreasing function of paper density.

By summing all the forces $F_{i,j}$ acting on the active fibers during each loading step, the force–displacement curve of the sample can be finally predicted.

4. Algorithmic aspects and model parameters' identification

The algorithmic aspects of the proposed model implemented in MATLAB R2022 are presented in Alg. 1. Note that $\texttt{Label}_{i,j}$ stands for the status of each fiber during loading steps and can assume four different values: 0, for a not yet recruited fiber; 1 for a recruited fiber; 2 for a debonded fiber; and 3 for a broken fiber. Therefore, the total number of activated, debonded and failed fibers can be estimated by summing the fibers of each class identified by the corresponding labels.

The following input data are required: (*i*) inputs concerning the geometry and the boundary conditions, (*ii*) inputs related to the fiber geometry, and (*iii*) inputs for the fiber mechanical properties. Concerning the first set of inputs, in this study we used three paper samples with different density. For these samples, we specified $B = 12.5$ mm, $L = 10.0$ mm and their respective thickness values are provided in Table 1.

Algorithm 1 Algorithm of the statistical mechanics model

Number of random realizations, N_g
Inputs for geometry and BCs: L, B, t, N_m, $w_{\max}$, isotropic/MD/CD
Inputs of the fibers' geometry: N_f, N_l, l_0, $l_{\max}$, d, μ_l, σ_l, μ_α, σ_α, $\lambda_{\min}$, λ_{avg}
Inputs of the fibers' mechanical properties: K, ϵ^{act}, $\epsilon^{\max}$, ϵ^{f}, r
for $s = 1, \dots, N_g$ **do** ▷ Loop over random realizations
  Construct the network:
  Random generation of fibers' length, orientation, number of bonds
  Position of fibers' coordinates $x_{i,j}^{(1)}$, $y_{i,j}^{(1)}$, $z_{i,j}^{(1)}$, $x_{i,j}^{(2)}$, $y_{i,j}^{(2)}$, $z_{i,j}^{(2)}$
  Compute $\epsilon_{i,j}^{a}$ and $\epsilon_{i,j}^{\max}$, Eqs. (4) and (8)
  Set $F = 0$, $\epsilon_{i,j} = 0$, $\text{d}\epsilon_{i,j} = 0$, $\texttt{Label}_{i,j} = 0$, $w = w_{\max}/N_m$
  for $m = 1, \dots, N_m$ **do**
    for $j = 1, \dots, N_l$ **do**
      for $i = 1, \dots, N_f$ **do**
        $\epsilon_{i,j} \leftarrow \epsilon + \text{d}\epsilon_{i,j}$
        if $\epsilon_{i,j} < \epsilon_{i,j}^{a}$ **then**
          $f_{i,j} \leftarrow 0$ ▷ Fiber not recruited
        end if
        if $\epsilon_{i,j} \geq \epsilon_{i,j}^{a}$ and $\epsilon_{i,j} < \min(\epsilon_{i,j}^{\max}, \epsilon^{\text{f}})$ **then**
          $\texttt{Label}_{i,j} \leftarrow 1$ ▷ Active fiber
          Compute $f_{i,j}$, Eq. (6)
          Finite elasticity update, Eqs. (10)
        end if
        if $\epsilon_{i,j} \geq \min(\epsilon_{i,j}^{\max}, \epsilon^{\text{f}})$ **then**
          if $\min(\epsilon_{i,j}^{\max}, \epsilon^{\text{f}}) = \epsilon_{i,j}^{\max}$ **then**
            $\texttt{Label}_{i,j} \leftarrow 2$ ▷ Debonded fiber
          end if
          if $\min(\epsilon_{i,j}^{\max}, \epsilon^{\text{f}}) = \epsilon^{\text{f}}$ **then**
            $\texttt{Label}_{i,j} \leftarrow 3$ ▷ Broken fiber
          end if
          $f_{i,j} \leftarrow 0$
          $\text{d}\epsilon_{i,j-1} \leftarrow \text{d}\epsilon_{i,j-1} + r/2\epsilon_{i,j}$
          $\text{d}\epsilon_{i,j+1} \leftarrow \text{d}\epsilon_{i,j+1} + r/2\epsilon_{i,j}$
        end if
        $F \leftarrow F + f_{i,j}$
      end for
    end for
    $\epsilon \leftarrow mw/L$
  end for
end for
Output: Stress-strain diagram, number of not recruited and recruited fibers, number of bonding and breakage failures.

For the paper configuration, the uni-axial tensile test was conducted in both the machine and the cross-machine directions of the tested specimens, and the maximum imposed strain for each sample was $w_{\max}/L$, see Table 1. Hence, a uniform strain $\epsilon = w/L$ has been applied in the proposed model in $N_m = 100$ loading steps with a linear ramp.

At the microscale, the use of the confocal microscope Leica DCM3D allows to visualize fibers and determine the required geometrical parameters of the model, such as N_f, N_l, $\lambda_{\min}$, λ_{avg}.

Fig. 7 shows an image of a paper specimen with $\rho = 1230$ (kg/m^3) captured using the confocal microscope with a 20× magnification, which is 637 × 477 μm size and contains a large number of fibers.

Thereby the number of fibers crossing an exemplary cross-section, e.g. the red line 477 μm long in Fig. 7, is counted to be 28, which gives a density of fibers 28/477 = 0.00587 fibers/μm and therefore a total number $N_f = 0.00587 \times B = 716$ of fibers in one layer for this sample.

In order to determine the number of layers within the paper specimen, N_l, we employed a methodology that relied on the assumption

Table 1
Paper samples properties and their boundary conditions.

Material	Paper density, ρ (kg/m^3)	Thickness, t (mm)	Maximum imposed strain, $w_{\max}/L$
1	697.0	0.2	0.085
2	737.7	0.1	0.050
3	1230.0	0.2	0.100

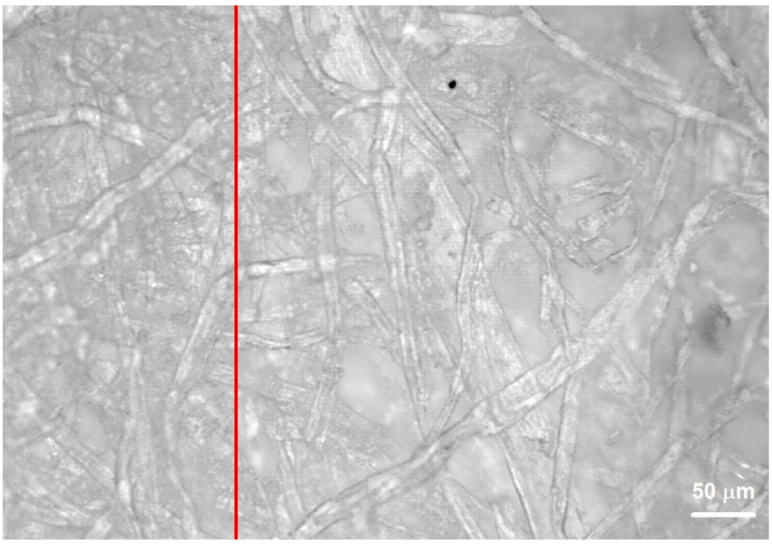

Fig. 7. Confocal microscope image of a paper sample with $\rho = 1230$ (kg/m^3) at 20× magnification, showing a random arrangement of cellulose fibers. The red line shows an exemplary cross-section.

that N_l corresponds to the count of fibers with large widths capable of fitting through the thickness of the specimen. To establish the average of maximum fiber width, $w_{\max}$, present in the sample, we employed a rigorous methodology that combined microscopy and image-processing techniques. The analysis involved the random selection of multiple snippets from the specimen, ensuring the inclusion of fibers with maximum widths. These snippets were carefully examined using a microscope and high-resolution images were captured. Leveraging the capabilities of the ImageJ software, we accurately measured the widths of the largest fibers in the selected snippets, accounting for the image scaling. To ensure statistical significance, measurements were taken for the largest fibers within each snippet. By averaging these measurements, we determined the average value for maximum fiber width to be 36.3 μm, for the samples of material 3, and consequently, 6 layers of fibers are packed through this sample thickness. Subsequently, the number of layers, N_l, and cross-sectional fibers, N_f, for two additional samples were derived; see Table 2, by scaling their corresponding thickness and density with the thickness and density of sample 3, respectively.

The parameters related to the free segment length, which are $\lambda_{\min}$, and λ_{avg} were determined experimentally: the ImageJ software was employed to calculate and compare the free distance between two bonds in each snippet, leading to the derivation of its minimum and the average values given in Table 2. It should be noted that determining these free segment lengths using a 2D image from confocal microscopy requires careful inspection of possible bonds. In this context, fibers that are crossing each other and observable on the surface are considered sufficiently pressed and therefore bonded when they belong to the same focal plane. For instance, in the area A of Fig. 8, fibers are in the same focal plane and can be considered in contact and bonded. Conversely, in the area B, fibers appear more blurry, belong to different focal planes, and are not sufficiently pressed to be bonded.

The other morphological parameters used for the proposed model are collected in Table 3, which were taken from the literature (the parameters related to the fibers' length and cross-section area are based on Kouko et al. (2020), the orientation parameter is based on Schulgasser (1985)).

Table 2
Fibers' geometry parameters derived from confocal microscopy.

Material	N_l	N_f	$\lambda_{\min}$ (μm)	λ_{avg} (μm)
1	6	406	7	48
2	3	859	6	45
3	6	716	6	37

Table 3
Fibers' geometry parameters taken from the literature.

$\mu_l \pm \sigma_l$ (mm)	l_0 (mm)	$l_{\max}$ (mm)	A (μm^2)	σ_α
2.5 ± 0.5	0.25	5	230	$\pi/2$

The last set of input data relates to the mechanical properties of fibers, a crucial and debatable aspect that requires a careful examination. The mechanical properties of cellulose fibers, such as Young modulus (E) and breakage strain of fibers (ϵ^{f}), exhibit variability in a network as reported in the literature (Maraghechi et al., 2023) based on single fiber tests. Kouko et al. (2020)'s experimental and micromechanical simulations emphasize the crucial role of fiber bonding in determining both the strength and elongation of fiber networks. To determine appropriate values for the mechanical parameters in our model, given the potential changes in these parameters during the paper-making process, we minimized the error between simulated and experimental stress–strain curves (Fig. 9) for each material, introducing a force redistribution factor (r) equal to 0.005 for all the cases (see the section on parametric analysis). The results of three replica for each material showed a very good repeatability of the experimental results, as illustrated in Fig. 9. The identified mechanical parameters for each material and sample are collected in Table 4. The identified Young modulus of fibers (E_f) resulted in values consistent with the range reported in recent experimental studies (Maraghechi et al., 2023). The maximum strain for fiber activation (ϵ^{act}) was identified to align with

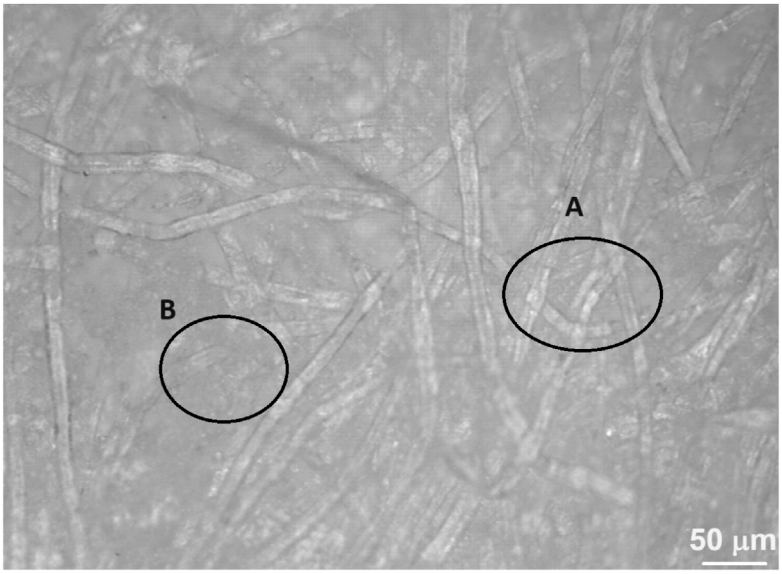

Fig. 8. Confocal microscope image of a paper sample with $\rho = 1230$ (kg/m^3) at 20× magnification. Fibers in the area "A" are considered bonded compared to the area "B", where fibers are blurry and belong to different focal planes.

Table 4
Identified properties of the model for the simulation results shown in Fig. 9.

Material	Sample	E_f (GPa)	ϵ^{max} (MD)	ϵ^{f} (MD)	ϵ^{max} (CD)	ϵ^{f} (CD)
1	1	31	0.022	0.031	0.0080	0.045
1	2	31	0.024	0.028	0.0080	0.058
1	3	31	0.023	0.028	0.0080	0.061
2	1	22	0.012	0.030	0.0055	0.037
2	2	22	0.010	0.026	0.0048	0.037
2	3	22	0.013	0.026	0.0045	0.037
3	1	21	0.020	0.047	0.0135	0.070
3	2	21	0.017	0.039	0.0130	0.060
3	3	21	0.019	0.045	0.0130	0.070

the nonlinear part of the experimental curve in the initial linear regime and has been set to 0.002 for all the materials. The maximum strain for debonding, ϵ^{max}, and the fiber breakage strain, ϵ^{f}, were determined by matching the second part of the experimental curves, where the steepness changes until reaching the peak.

Results shown in Table 4 highlight that fiber stiffness is independent of the specimen tested, while it depends upon the material density. Parameters related to the failure strain, ϵ^{max} and ϵ^{f}, are dependent not only on the specimen tested, but also on the material density. On the other hand, variations in papermaking conditions, such as drying process, can impact the mechanical properties of paper materials. Notably, the mechanical properties of fibers in the machine direction (MD) and cross-machine direction (CD) may differ due to distinct drying conditions in those directions. Research presented by Wahlstrom (1999) indicates that reducing shrinkage or applying stretch significantly decreases the strain at break, potentially explaining the lower values of ϵ^{f} in the MD direction as compared to those in the CD direction. The variability in the debonding strain, ϵ^{max}, could be subject to changes during the papermaking process as well.

A simple guideline on how to identify the mechanical model parameters from an experimental uniaxial stress–strain curve is provided in Fig. 10. The activation strain ϵ^{act} has a specific role on the recruitment of fibers and on the nonlinear response for very small strains. Then, the fiber stiffness K influences the slope of the linear regime. The parameter ϵ^{max} is modulating the transition from linear elastic to ipoelastic regimes, and finally ϵ^{f} is the strain at the peak of the diagram, at the onset of catastrophic failure.

The model provides further insight into the effect of paper anisotropy due to fiber orientation resulting from the machining process, which leads to distinct characteristics along the machine direction (MD) and the cross-machine direction (CD). The total number of fibers in a cross-section of the network model comprises the sum of not-activated fibers, activated fibers, and failed fibers (including both broken and debonded fibers). We remark that the sum of the percentages of fibers in different states (active, not-active, debonded and broken in Figs. 11), for each material in a given configuration (MD or CD), always amount to 100% at any strain level, which is the total number of fibers of the cross-section.

Simulation results, depicted in Figs. 11(a), 11(c), and 11(e), compare the percentage of fibers that become active during the test in the MD and CD cases for material 1, 2, and 3 respectively. In the MD configuration, around 70% of fibers were recruited and activated during the loading process, for all the materials with different paper densities. This can be explained by the fact that loading the specimen along the machine direction, which has the majority of fibers oriented in the same direction, accelerates reaching the activation strain required to contribute to load transfer. In contrast, for the CD configuration, lower percentages of fibers between 40% and 50% are recruited, since most of the fibers are not aligned along the direction of loading. Moreover, in the case of material 3, the difference between the percentages of active fibers for the MD and CD directions is smaller than in the other materials, indicating a lower degree of anisotropy for it.

Furthermore, the model offers predictive insights into the evolution of the percentage of failed fibers during loading, considering both debonding and breakage. As depicted in Figs. 11(b), 11(d), and 11(f), the total number of failed fibers, encompassing both debonded and broken fibers, is higher in the MD direction across all samples. Significantly, the simulations show that paper fracture predominantly occurs due to debonding in both the MD and CD configurations, with the count of broken fibers in the CD being much lower than in the MD. This correlates with Johansson et al. (2021) findings, indicating internal delamination as the primary failure mode in CD-tested samples, further supporting our observation of fewer broken fibers in the CD as compared to the MD.

Fig. 12 illustrates the probability distribution of the mean free length, λ, and of the fiber failure strain, ϵ^{f} ($\epsilon^{max}_{i,j}$ and ϵ^{f}), in the CD direction for the three materials herein analyzed. Material 3, characterized by the highest density, has a λ distribution exhibiting a lower

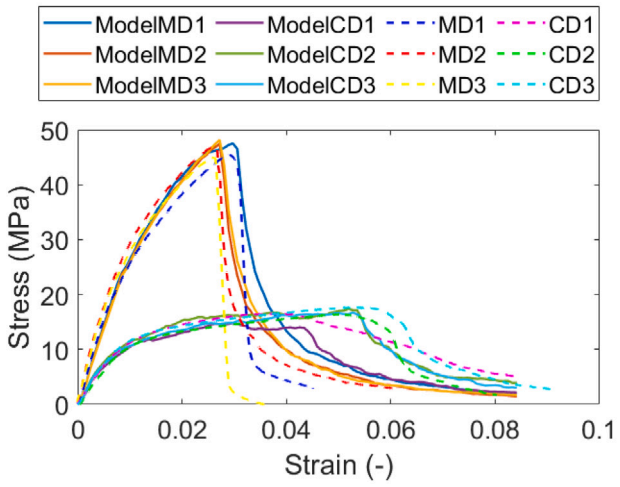

(a) Material 1, $\rho = 697.0$ kg/m^3

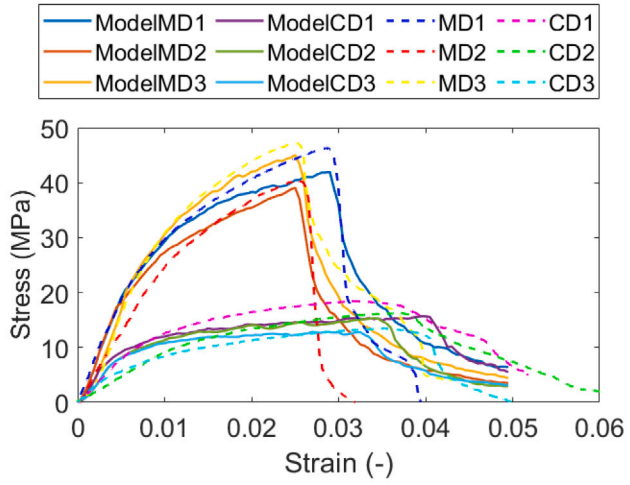

(b) Material 2, $\rho = 737.7$ kg/m^3

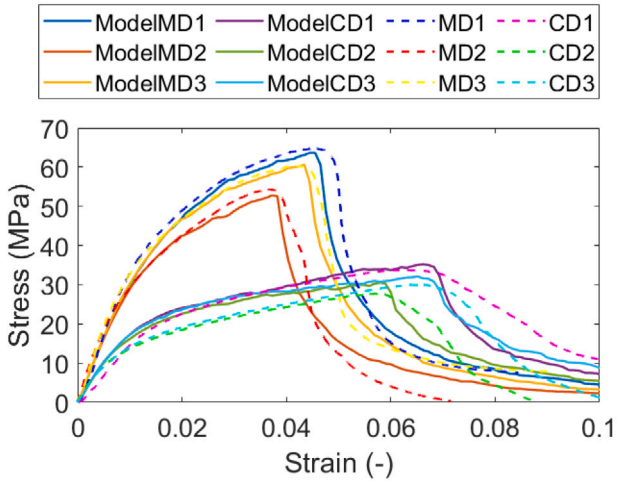

(c) Material 3, $\rho = 1230.0$ kg/m^3

Fig. 9. Simulated (solid lines) and experimental (dashed lines) stress–strain curves of the paper materials with different densities. Each material had three repetitions of the test.

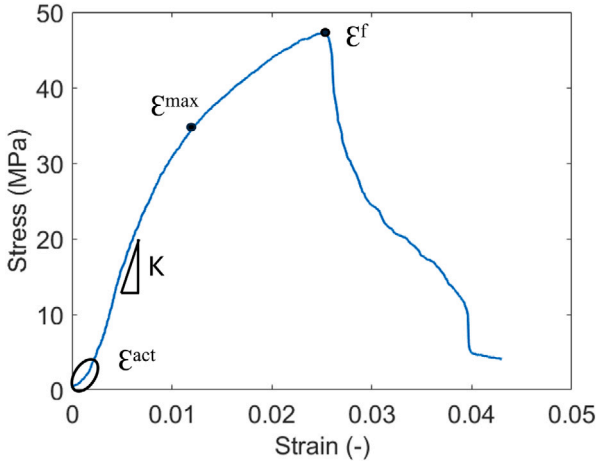

Fig. 10. Guideline for the identification of model parameters based on experimental stress–strain curves.

average value, indicating denser regions near $\lambda_{\min}$. This implies that denser papers have a higher probability of having λ close to zero and a lower probability of having large λ, resulting in reduced porosity and enhanced strength, consistent with the maximum tensile stress and maximum elongation at the peak point in Fig. 9. The distribution of ϵ^f is influenced not only by the λ distribution but also by the papermaking process. Surprisingly, materials 1 and 2, with similar densities, show distinct ϵ^f distributions, possibly attributed to layer effects. Conversely, materials 1 and 3, despite having significantly different densities, exhibit similar ϵ^f distributions, likely due to their equal thicknesses.

A crucial question arises concerning the observed changes in the slope of the stress–strain curve in our model, given that we have considered a linear constitutive relation for fibers, encompassing their elastic behavior. To address this, we present the stress–strain curves of material 1 alongside the percentage of failed fibers (the sum of debonded and broken fibers shown in Fig. 11(b)) vs. strain in Fig. 13. This figure clarifies that the alteration in the slope of the stress–strain curve in both MD and CD directions is attributed to the increasing number of failed fibers beyond certain strains. In the CD configuration, fibers begin debonding from a strain of approximately 0.01 until the peak point. Subsequently, the slope of failed fibers increases, signifying a significant decrease in the number of fibers capable of bearing the load and, consequently, leading to the observed post-peak behavior in the stress–strain curve. Interestingly, in the MD direction, the number of failed fibers is initially lower than in the CD configuration until the peak load is reached. However, it significantly increases afterward, surpassing the CD's count, resulting in a sharp decline in the MD stress–strain curve. This is due to the parameter ϵ^{f} which differs between MD and CD directions because of variations in papermaking conditions. These variations result in fibers being more brittle in the MD, leading to have significantly higher percentage of broken fibers in the MD compared to the CD.

An additional test under cyclic loading conditions with variable strain amplitudes has been conducted to confirm some key assumptions of the proposed model. The analysis of the cyclic stress–strain curves provides the amount of *recovered strain* during unloading, see the sketch in Fig. 14 for its computation.

Specifically, material 3 was tested both in the MD and CD directions by applying uniaxial tensile loading to the samples until reaching predetermined strains, incrementally increased by steps of about 20% from zero to the strain at the peak load. Subsequently, the samples underwent unloading to zero load, followed by reloading. The results of these tests are shown in Fig. 15(a). Based on the proposed model, at unloading we expect to have an amount of recovered strain associated to the active fibers that at the unloading strain had a linear elastical behavior. On the other hand, the amount of irreversible strain not

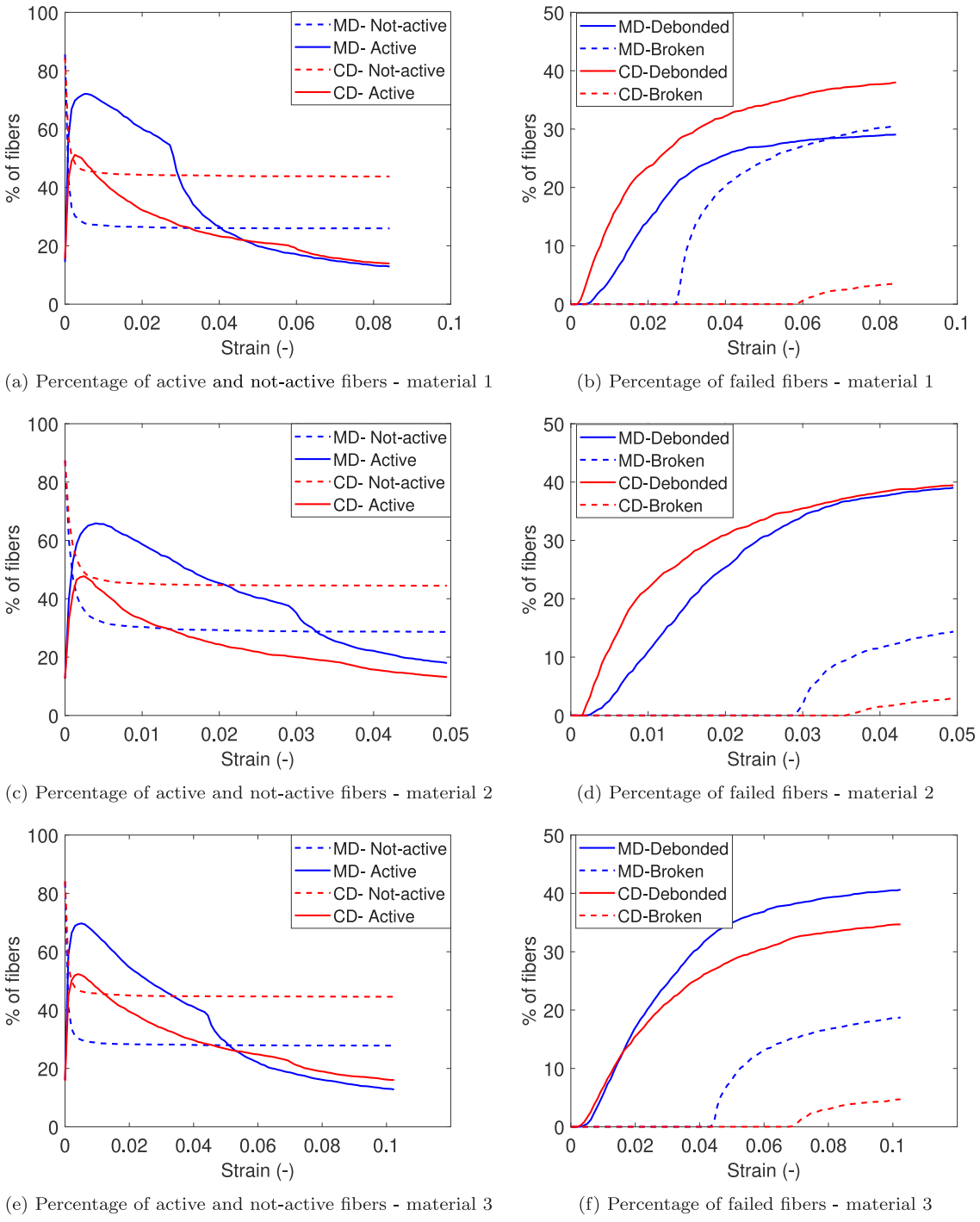

(a) Percentage of active and not-active fibers - material 1

(b) Percentage of failed fibers - material 1

(c) Percentage of active and not-active fibers - material 2

(d) Percentage of failed fibers - material 2

(e) Percentage of active and not-active fibers - material 3

(f) Percentage of failed fibers - material 3

Fig. 11. a, c, and e: Percentage of active and not-active fibers during a uniaxial tensile test of paper materials 1, 2, and 3 respectively. b, d, and f: Percentage of failed fibers (debonded and broken) during loading for materials 1, 2, and 3, respectively, for both the MD and CD configurations.

recovered during unloading is caused by those fibers that achieved debonding failure. Therefore, the *expected recovered strain* provided by the model should be equal to:

$$\epsilon_r = \epsilon_{\text{un}} \left(\frac{N_a}{N_t} \right) \tag{11}$$

where ϵ_{un} is the strain at the point of unloading, N_a is the number of linear elastic active fibers at that point, and N_t is the total number of fibers. The comparison between the expected (model predicted) recovered strains and the experimentally observed recovered strains at different levels of unloading strain is shown in Fig. 15(b). Remarkably, the results demonstrate that the two set of data are closely aligned on the 45° line shown in black, which implies that the model is accurately predicting the amount of recovered strain measured in the experiments and, as a consequence, it confirms the ability of the model to correctly predict the evolution of active fibers with loading and the underlying model assumptions.

5. Sensitivity analysis

To further assess the robustness of the developed statistical mechanics model and further understand the effect of each model parameter, a

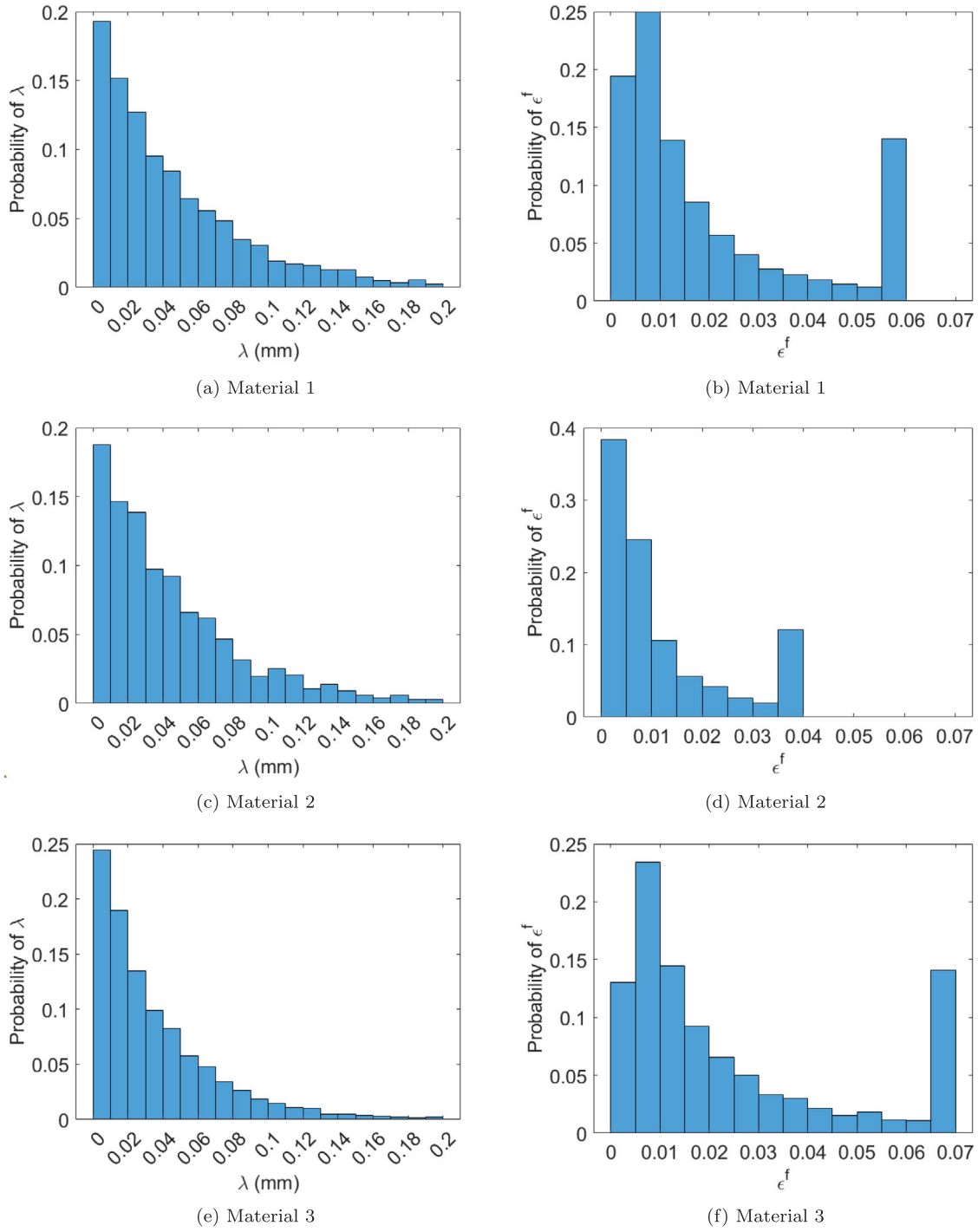

(a) Material 1 (b) Material 1

(c) Material 2 (d) Material 2

(e) Material 3 (f) Material 3

Fig. 12. a, c, e : Probability distribution of mean free length in materials 1, 2, and 3 respectively. b, d, f : Distribution of failure strain of fibers in the cross-machine direction in materials 1, 2, and 3 respectively.

sensitivity analysis is herein put forward. It is important to note that the parameters employed in this analysis are specifically related to material 1, ensuring a focused examination of its sensitivity to variations in these key factors.

The first aspect investigated is the effect of randomness of the network for the set of parameters identified in the previous section. As previously outlined, in fact, the proposed model involves the construction of networks along the critical cross-section comprising fibers characterized by stochastic variations in length, orientation, and mean free path. The model is not a pure cross-sectional model, since the parameters include also the free segment length of the fibers, which is an additional information relevant for this type of networks and includes longitudinal features of the network. This allows for a more comprehensive analysis that acknowledges the non-affine behavior introduced by phenomena like fiber recruitment and debonding failure. To evaluate the impact of this randomness, we repeated a series of 100 simulations by extracting the parameters of the fibers from the statistical distributions in each run. Fig. 16 presents the mean value of these simulations (dashed line) accompanied by a shaded region representing the standard deviation from the mean. Results show that the underlying randomness of the network properties have a minimal

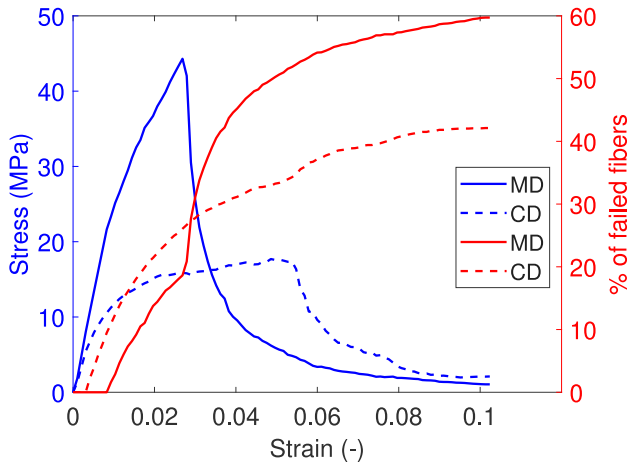

Fig. 13. Experimental stress–strain curve of material 1, blue curves, accompanied by the corresponding failed fibers percentage relative to strain, red ones, in the both MD and CD directions.

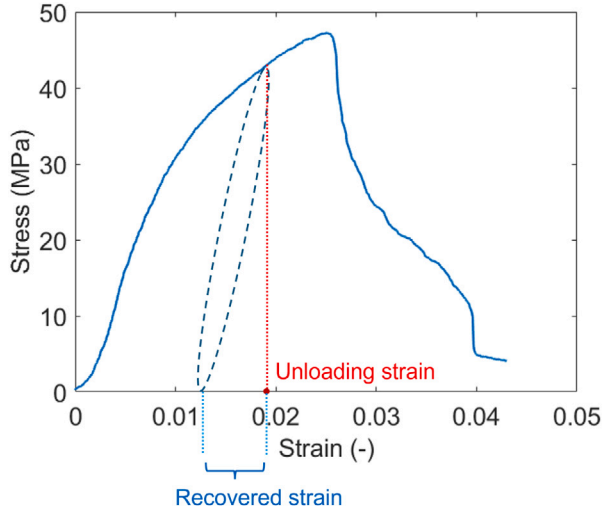

Fig. 14. Measurement of the recovered strain from cyclic loading tests.

influence on the model outcomes due to the large size of the fibers accounted in the model.

Previous results in the literature (Kouko et al., 2020) showed that the macroscopic mechanical behavior of paper is strongly influenced by the inter-fiber bond strength and fiber elongation. To gain an insight into these effects, we conducted simulations with three distinct values of $\epsilon^{\max}$: 0.01, 0.015, and 0.022. High values of this parameter can be obtained by exerting a higher pressure during wet pressing of paper, or by adding some chemical additives to increase bonding during the production process. Simulation results are shown in Fig. 17(a) and clearly demonstrate that the strength of fiber-to-fiber bonds has a profound effect on the overall strength of paper materials, without significantly altering the initial stiffness and the ductility of the paper specimen. This result can be explained by the fact that fibers requiring a higher strain to debond contribute more substantially to the load-bearing capacity of the paper. Consequently, papers with stronger inter-fiber bonds exhibit higher maximum forces at the point of failure.

The influence of fiber elongation at failure, on the other hand, has been analyzed by simulating three networks with ϵ^{f} equal to 0.028, 0.04 and 0.06, while keeping other parameters constant. The outcomes of these simulations shown in Fig. 17(b) pinpoint that this parameter has a strong impact on paper ductility and also on the load-carrying capacity.

The mechanical properties of fibers, which eventually affect the fibers' stiffness K in the present model, can be changed during papermaking process by adding additives or in case of recycled fibers (Hubbe et al., 2007; Kouko et al., 2019; Motamedian et al., 2019). Results of simulations of fiber networks with different values of the Young's modulus equal to 11, 21, and 31 GPa are shown in Fig. 18. Stiffer fibers result in networks with increased stiffness and also a higher peak force. This outcome not only provides valuable insights into the underlying mechanics of paper materials but also carries practical significance. Specifically, it implies that according to Hubbe et al. (2007), since recycled papers characterized by enhanced fiber stiffness compared to the virgin one, could possess the potential for greater mechanical robustness.

The role played by strain redistribution, which essentially means that when one fiber of the simulated paper network fails some of its strain is redistributed to its neighboring fibers, is herein analyzed. In the present model, redistribution has been confined to the closest fiber neighbors, but it could be extended to include a wider non-locality. Fig. 19 shows three force–displacement curves, each one representing a paper network response under tensile loading with three different strain redistribution factors $r = 0.005$, 0.08, and 0.2. Higher strain redistribution anticipates the achievement of the peak load and, at the same time, it flattens the curve before the softening branch.

6. Conclusion

In order to understand the micro-structural mechanisms governing the fracture behavior of paper materials, we conducted a campaign of in-situ tensile tests using the DEBEN micro-mechanical tensile stage combined with the confocal microscope Leica DCM3D. This setup enables the simultaneous visualization of the cellulose fibers' deformation during the loading process, observing microstructural mechanisms such as fiber activation and recruitment, fiber debonding and fiber failure. Notably, these individual mechanisms are found to be dependent on the fiber average free length between subsequent bonds.

Inspired by our experimental findings, we proposed a stochastic mechanics model as a valuable tool for comprehensively examining the mechanical response of paper sheets under uniaxial loading. The model clearly decouples the information on the topology of the fiber network from the mechanical constitutive response of each single fiber. Micro-geometrical data that can be identified from microscopy images include the new morphological parameter called mean free path λ between two subsequent bonds, the mean fiber diameter, the fiber orientation and the fiber length, in addition to the number of fibers along the simulated critical cross-section. Fiber orientation and fiber length are considered as random fields obeying a Gaussian distribution. The mean free path is also modeled as a random field obeying an exponential distribution with an average value that can be estimated from images. Through the functional dependencies of the model, the activation strain and the failure strain of the fibers become random fields as well. The constitutive model of the fibers has been considered as linear elastic. It has to be remarked that the model is not a pure cross-sectional model, since the parameters include the free segment length of the fibers which is an additional information relevant for this type of networks and accounts for longitudinal features of the network. This allows for a more comprehensive analysis that acknowledges the non-affine behavior introduced by phenomena like fiber recruitment and debonding failure.

The model parameters were determined based on three paper materials with different densities, aligning the simulation outcomes with the corresponding experimental results for each sample. The simulations emphasized the critical influence of density and the papermaking process on the strength of paper materials, showcasing substantial changes in mechanical properties. Furthermore, the simulations highlighted that paper fracture predominantly arises from fiber debonding rather than breakage, especially in the cross-machine direction (CD). The disparity

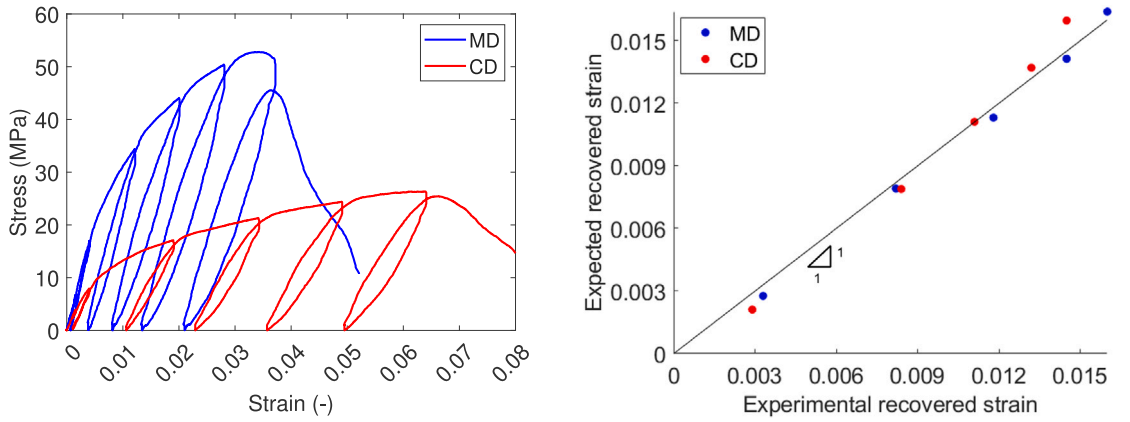

(a) (b)

Fig. 15. (a) Stress–strain curves from cyclic tests with variable amplitude strain conducted on Material 3 inthe MD and CD directions. (b) Expected vs. and experimentally measured recovered strains at zero stress during unloading.

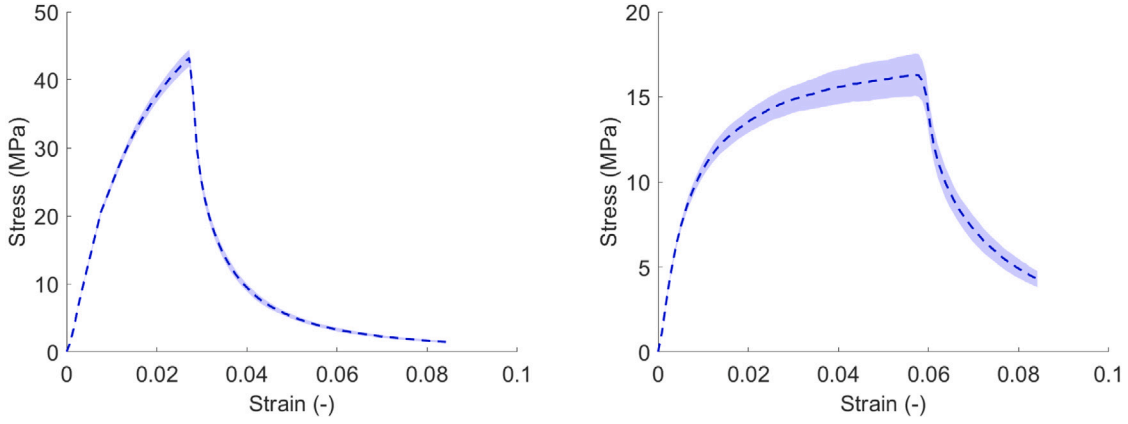

(a) Loading in the machine direction (b) Loading in the cross-machine direction

Fig. 16. Mean stress–strain diagram over 100 simulations (dashed line); the shaded area represents the envelope related to the standard variation from the mean value.

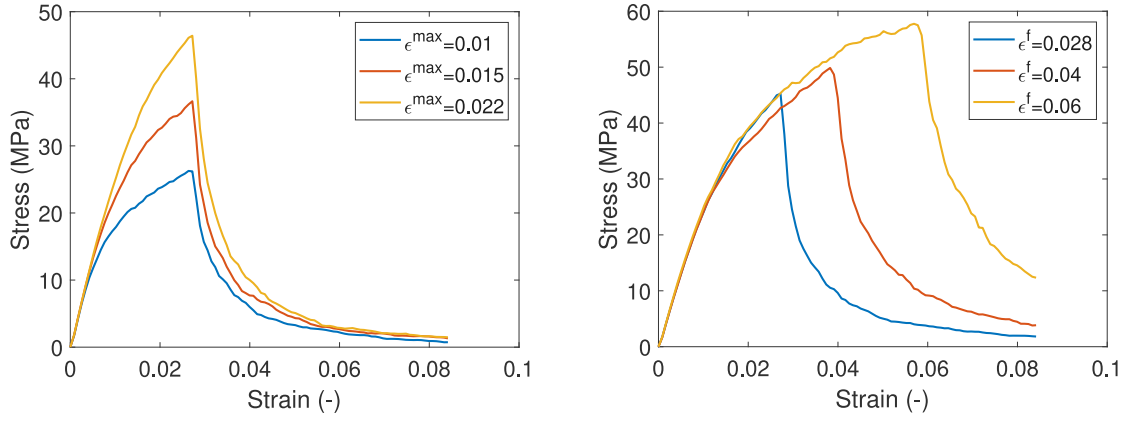

(a) Effect of $\epsilon^{\max}$ (b) Effect of ϵ^{f}

Fig. 17. Effect of (a) inter-fiber bond strength, and (b) fiber elongation at failure.

in the number of active fibers between the MD and CD configurations contributes to the anisotropy observed in paper materials. Additionally, an investigation into the changes in the slope of stress–strain curve was conducted by correlating it with the percentage of failed fibers versus strain.

The sensitivity analysis led to the observation that the inter-fiber bond strength and the fiber elongation at failure are significantly affecting the overall mechanical response. The constitutive model of the fibers also plays an important role, in which the Young modulus of the fibers significantly influences the paper stiffness and the peak force. Redistribution effects, on the other hand, impact on the shape of the stress–strain curve near the peak load, with an increased smoothing and flattening of the curve for higher values of r.

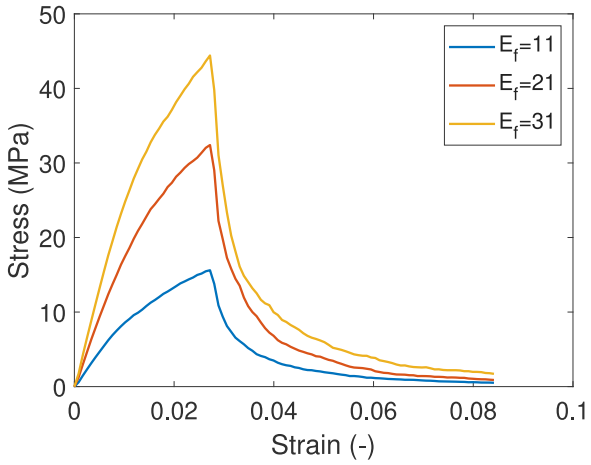

Fig. 18. The effect of the Young's modulus of fibers.

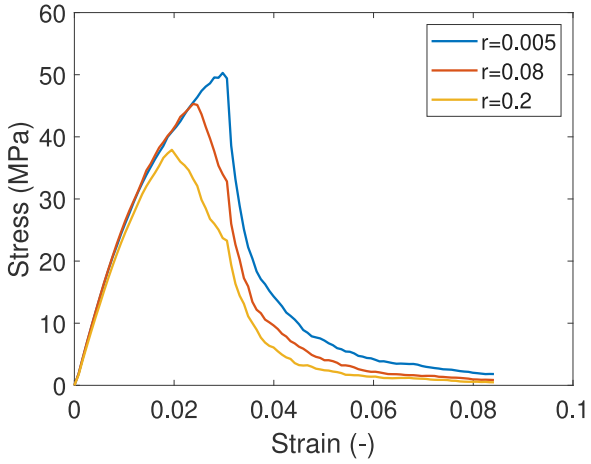

Fig. 19. Stress–strain curves of a paper network under tensile loading with different strain redistribution factors ($r = 0.005$, 0.08, 0.2).

CRediT authorship contribution statement

Mohadeseh Fallah: Writing – original draft, Validation, Software, Methodology, Conceptualization. **Hamed Zarei:** Writing – original draft, Software, Methodology, Conceptualization. **Marco Paggi:** Writing – original draft, Validation, Supervision, Software, Methodology, Conceptualization.

Declaration of competing interest

The authors declare that they have no known competing financial interests or personal relationships that could have appeared to influence the work reported in this paper.

Data availability

Data will be made available on request.

Declaration of generative AI in scientific writing

No generative AI technologies have been used in this work.

Appendix A. Supplementary data

Supplementary material related to this article can be found online at https://doi.org/10.1016/j.ijsolstr.2024.112930.

References

Alava, M., Niskanen, K., 2006. The physics of paper. Rep. Progr. Phys. 69 (3), 669.
Borodulina, S., Kulachenko, A., Nygårds, M., Galland, S., 2012. Stress-strain curve of paper revisited. Nordic Pulp Pap. Res. J. 27 (2), 318–328.
Borri, C., Paggi, M., Reinoso, J., Borodich, F., 2016. Adhesive behaviour of bonded paper layers: Mechanical testing and statistical modelling. Proc. Inst. Mech. Eng. C 230, 1440—-1448.
Brandberg, A., Österling, S.R., Kulachenko, A., Hirn, U., 2022. Characterization and impact of fiber size variability on the mechanical properties of fiber networks with an application to paper materials. Int. J. Solids Struct. 239, 111438.
Cox, H.L., 1952. The elasticity and strength of paper and other fibrous materials. Br. J. Appl. Phys. 3 (3), 72.
Dodson, C., Sampson, W., 1999. Spatial statistics of stochastic fiber networks. J. Stat. Phys. 96, 447–458.
El-Hosseiny, F., Page, D., 1975. The mechanical properties of single wood pulp fibres: theories of strength. Fibre Sci. Technol. 8 (1), 21–31.
Gizzi, A., Vasta, M., Pandolfi, A., 2014. Modeling collagen recruitment in hyperelastic bio-material models with statistical distribution of the fiber orientation. Internat. J. Engrg. Sci. 78, 48–60.
Groom, L.H., Mott, L., Shaler, S., 2002. Mechanical properties of individual southern pine fibers. Part I. Determination of variability of stress-strain curves with respect to tree height and juvenility. Wood Fiber Sci. 34 (1), 14–27.
He, X., Lu, J., 2022. Explicit consideration of fiber recruitment in vascular constitutive formulation using beta functions. J. Mech. Phys. Solids 163, 104837.
Hubbe, M.A., Venditti, R.A., Rojas, O.J., 2007. What happens to cellulosic fibers during papermaking and recycling? A review. BioResources 2 (4), 739–788.
Johansson, S., Engqvist, J., Tryding, J., Hall, S., 2021. 3D strain field evolution and failure mechanisms in anisotropic paperboard. Exp. Mech. 61, 581–608.
Johansson, S., Engqvist, J., Tryding, J., Hall, S.A., 2022. Microscale deformation mechanisms in paperboard during continuous tensile loading and 4D synchrotron X-ray tomography. Strain 58 (5), e12414.
Kloppenburg, G., Li, X., Dinkelmann, A., Finckh, H., Neumann, J., Simon, J.-W., 2023a. Identifying microstructural properties of paper. PAMM 23 (3), e202300251.
Kloppenburg, G., Walther, E., Holthusen, H., Czibula, C., Hirn, U., Simon, J.-W., 2023b. Using numerical homogenization to determine the representative volume element size of paper. PAMM 22 (1), e202200226.
Kouko, J., Jajcinovic, M., Fischer, W., Ketola, A., Hirn, U., Retulainen, E., 2019. Effect of mechanically induced micro deformations on extensibility and strength of individual softwood pulp fibers and sheets. Cellulose 26, 1995–2012.
Kouko, J., Turpeinen, T., Kulachenko, A., Hirn, U., Retulainen, E., 2020. Understanding extensibility of paper: role of fiber elongation and fiber bonding. Tappi J. 19 (3), 125–135.
Kulachenko, A., Uesaka, T., 2012. Direct simulations of fiber network deformation and failure. Mech. Mater. 51, 1–14.
Li, K., Holzapfel, G.A., 2019. Multiscale modeling of fiber recruitment and damage with a discrete fiber dispersion method. J. Mech. Phys. Solids 126, 226–244.
Li, Y., Stamleton, S.E., Reese, S., Simon, J.-W., 2016. Multiscale modeling of paper. In: 17th European Conference on Composite Materials.
Li, Y., Yu, Z., Reese, S., Simon, J.-W., 2018. Evaluation of the out-of-plane response of fiber networks with a representative volume element model. Tappi J. 17 (6), 329–339.
Magnusson, M.S., Zhang, X., Östlund, S., 2013. Experimental evaluation of the interfibre joint strength of papermaking fibres in terms of manufacturing parameters and in two different loading directions. Exp. Mech. 53, 1621–1634.
Maraghechi, S., Bosco, E., Suiker, A.S., Hoefnagels, J.P., 2023. Experimental characterisation of the local mechanical behaviour of cellulose fibres: an in-situ micro-profilometry approach. Cellulose 30 (7), 4225–4245.
Marengo, A., 2023. The Phase-Field Modeling of Fracture Evolution in Ductile Materials with Application to Paperboard Mechanics. (Ph.D. thesis). Politecnico di Milano, Milano, Italy.
Motamedian, H.R., Halilovic, A.E., Kulachenko, A., 2019. Mechanisms of strength and stiffness improvement of paper after PFI refining with a focus on the effect of fines. Cellulose 26, 4099–4124.
Niskanen, K., 2011. Mechanics of Paper Products. Walter de Gruyter.
Paggi, M., Reinoso, J., 2015. An anisotropic large displacement cohesive zone model for fibrillar and crazing interfaces. Int. J. Solids Struct. 69–70, 106–120.
Pradhan, S., Hansen, A., Chakrabarti, B.K., 2010. Failure processes in elastic fiber bundles. Rev. Modern Phys. 82 (1), 499.
Pugno, N.M., Bosia, F., Abdalrahman, T., 2012. Hierarchical fiber bundle model to investigate the complex architectures of biological materials. Phys. Rev. E 85 (1), 011903.
Schulgasser, K., 1985. Fibre orientation in machine-made paper. J. Mater. Sci. 20, 859–866.
Shahsavari, A., Picu, R., 2013. Size effect on mechanical behavior of random fiber networks. Int. J. Solids Struct. 50 (20–21), 3332–3338.
Simon, J.-W., 2021. A review of recent trends and challenges in computational modeling of paper and paperboard at different scales. Arch. Comput. Methods Eng. 28 (4), 2409–2428.

Tojaga, V., Kulachenko, A., Östlund, S., Gasser, T.C., 2021. Modeling multi-fracturing fibers in fiber networks using elastoplastic timoshenko beam finite elements with embedded strong discontinuities—Formulation and staggered algorithm. Comput. Methods Appl. Mech. Engrg. 384, 113964.

Torgnysdotter, A., Kulachenko, A., Gradin, P., Wågberg, L., 2007a. Fiber/fiber crosses: finite element modeling and comparison with experiment. J. Compos. Mater. 41 (13), 1603–1618.

Torgnysdotter, A., Kulachenko, A., Gradin, P., Wågberg, L., 2007b. The link between the fiber contact zone and the physical properties of paper: a way to control paper properties. J. Compos. Mater. 41 (13), 1619–1633.

Wahlstrom, T., 1999. Influence of shrinkage and stretch during drying on paper properties, KTH licentiate thesis.

Yi, Y., Berhan, L., Sastry, A.M., 2004. Statistical geometry of random fibrous networks, revisited: waviness, dimensionality, and percolation. J. Appl. Phys. 96 (3), 1318–1327.